ENVIRONMENTAL STUDIES

Quantifying methane emissions from the largest oil-producing basin in the United States from space

Yuzhong Zhang[1,2,3,4]*, Ritesh Gautam[2]*, Sudhanshu Pandey[5], Mark Omara[2],
Joannes D. Maasakkers[5], Pankaj Sadavarte[5,6], David Lyon[2], Hannah Nesser[1], Melissa P. Sulprizio[1],
Daniel J. Varon[1], Ruixiong Zhang[7,8], Sander Houweling[5,9], Daniel Zavala-Araiza[2,10],
Ramon A. Alvarez[2], Alba Lorente[5], Steven P. Hamburg[2], Ilse Aben[5], Daniel J. Jacob[1]

Using new satellite observations and atmospheric inverse modeling, we report methane emissions from the Permian Basin, which is among the world's most prolific oil-producing regions and accounts for >30% of total U.S. oil production. Based on satellite measurements from May 2018 to March 2019, Permian methane emissions from oil and natural gas production are estimated to be 2.7 ± 0.5 Tg a^{-1}, representing the largest methane flux ever reported from a U.S. oil/gas-producing region and are more than two times higher than bottom-up inventory-based estimates. This magnitude of emissions is 3.7% of the gross gas extracted in the Permian, i.e., ~60% higher than the national average leakage rate. The high methane leakage rate is likely contributed by extensive venting and flaring, resulting from insufficient infrastructure to process and transport natural gas. This work demonstrates a high-resolution satellite data–based atmospheric inversion framework, providing a robust top-down analytical tool for quantifying and evaluating subregional methane emissions.

INTRODUCTION

Methane is a potent greenhouse gas with a relatively short average atmospheric residence time of about a decade and is also a precursor of tropospheric ozone (1). The emission-based radiative forcing for methane (including effects on tropospheric ozone and stratospheric water vapor) is 0.97 W m^{-2} since preindustrial times, which is about 60% of that for CO$_2$ (2). Roughly a third of the contemporary anthropogenic methane emissions come from the fossil fuel energy sector worldwide (oil, natural gas, and coal) (~100 to 180 Tg a^{-1}) (3, 4, 5). Curbing anthropogenic methane emissions, including those from the oil/gas sector, is considered an effective strategy to slow the rate of near-term climate warming (1). However, the rapid increase in oil and natural gas (O/G) production in the United States since around 2005, driven primarily by hydraulic fracturing and horizontal drilling, has led to major concerns about increasing methane emissions and adverse climate impacts (6). By upscaling data collected from field measurements in some of the largest O/G production basins in the United States, Alvarez et al. (7) estimated 13 Tg annual methane emissions from the national O/G supply chain for 2015, which is 60% higher than the official estimates by the U.S. Environmental Protection Agency (EPA) (8). The largest discrepancy was found in the O/G production segment where the estimate by Alvarez et al. (7) (7.6 Tg a^{-1}) was more than two times that by EPA, which relies on inventory-based estimates (3.5 Tg a^{-1}) (8).

While field measurements provide in-depth information about a particular site or area, it is often challenging to expand the measurement capacity to observe a diverse set of targets distributed globally over longer periods of time. Additional challenges exist for areas that are difficult to access for technical or proprietary reasons. On the other hand, global satellite observations of column atmospheric methane offer a unique vantage point to identify emission hot spots and quantify regional emissions (9). Using data from SCanning Imaging Absorption spectroMeter for Atmospheric CHartographY (SCIAMACHY) satellite observations averaged between 2003 and 2009, Kort et al. (10) found large anomalous methane levels from the Four Corners region in the United States, with total methane emissions associated with natural gas, coal, and coalbed sources estimated as 0.59 ± 0.08 Tg a^{-1}. While the SCIAMACHY data were fairly limited in spatial resolution (30 km × 60 km) and measurement precision [30 parts per billion in volume or (ppbv)] (9), it was the first time that satellite observations were used to quantify a dense O/G-related methane emission hot spot. This finding also led to several dedicated airborne studies to better understand methane sources in the region (11, 12), which reported methane fluxes comparable to the satellite-based estimate (10).

Here, we demonstrate and exploit the capability of a recent spaceborne sensor, the Tropospheric Monitoring Instrument (TROPOMI), to map atmospheric methane enhancements in the United States and quantify emissions from the Permian Basin (Fig. 1), which has become one of the world's most prolific oil-producing regions in recent years due to advances in drilling technologies. Located in New Mexico and Texas in a region of ~400 km × 400 km, Permian is currently the largest oil-producing basin in the United States. In 2018, the Permian Basin produced 5.5×10^5 m^3 (or 3.5 million barrels) of crude oil and 3.2×10^8 m^3 (or 11 billion feet^3) of natural gas every day (~30 and ~10% of the U.S. national totals, respectively), which was 4 and 2.5 times their corresponding levels in 2007 (around the time of SCIAMACHY observations) (Fig. 2) (13). While the surging production in the Permian Basin and its importance in the U.S. oil boom during the last decade have been widely covered in mass

[1]School of Engineering and Applied Sciences, Harvard University, Cambridge, MA 02138, USA. [2]Environmental Defense Fund, Washington, DC 20009, USA. [3]School of Engineering, Westlake University, Hangzhou, Zhejiang Province, China. [4]Institute of Advanced Technology, Westlake Institute for Advanced Study, Hangzhou, Zhejiang Province, China. [5]SRON Netherlands Institute for Space Research, Utrecht, Netherlands. [6]TNO, Department of Climate, Air and Sustainability, Utrecht, Netherlands. [7]School of Earth and Atmospheric Sciences, Georgia Institute of Technology, Atlanta, GA 30332, USA. [8]ClimaCell Inc., 280 Summer Street Floor 8, Boston, MA 02210, USA. [9]Department of Earth Sciences, Vrije Universiteit Amsterdam, Amsterdam, Netherlands. [10]Institute for Marine and Atmospheric Research Utrecht (IMAU), Utrecht University, Utrecht, Netherlands.
*Corresponding author. Email: zhangyuzhong@westlake.edu.cn (Y.Z.); rgautam@edf.org (R.G.)
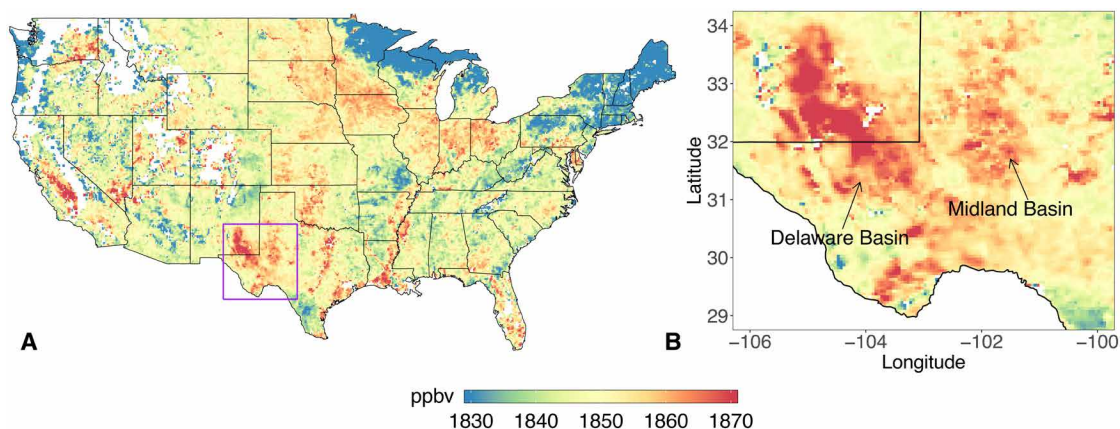
Fig. 1. Satellite observations of the Permian methane anomaly. TROPOMI satellite data derived elevation-corrected column methane mixing ratio for (**A**) the conterminous United States and (**B**) the Permian Basin containing the Delaware and Midland sub-basins. White shading represents missing data. Purple boundary in (A) indicates the study domain encompassing the Permian Basin. Methane averages are computed from monthly means of TROPOMI measurements during May 2018 and March 2019.
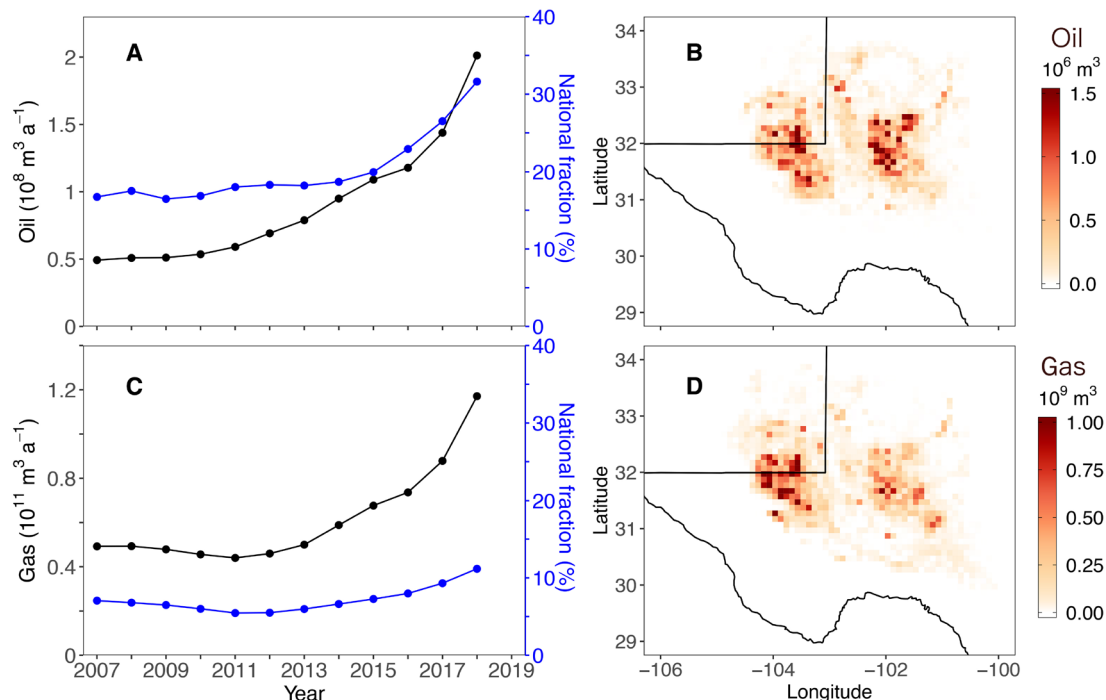
Fig. 2. Oil and gas production in the Permian Basin. (**A** and **C**) Time series of annual O/G production in black and the corresponding fractions of total U.S. production in blue [data from the Drilling Productivity Report by EIA (*13*)]. (**B** and **D**) Spatial distribution of oil and gas production for 2018 [data from Enverus Drillinginfo (*50*)]. Oil production includes both crude and condensate production. Gas production represents gross (before processing) gas production.

media (*14*), the scale of associated methane emissions from this critical O/G basin is unknown, despite reports of increased flaring and venting activity (*15*).

Using 11 months of recent data acquired by TROPOMI during 2018–2019, we focus on the distinct methane concentration anomaly over the Permian Basin and quantify the associated methane emissions with a state-of-the-art atmospheric inverse modeling framework. TROPOMI was launched in October 2017 onboard the European Space Agency's Sentinel-5P satellite and provides column atmospheric methane measurements with higher spatial resolution (7 km × 7 km at nadir) and precision (0.6%) than was previously available (*16*), providing near-daily global coverage with its large 2600-km-wide

swath (*17*). Our integrated satellite-based approach provides new insights into the dynamic landscape of O/G-related methane emissions in the United States and should pave the way forward toward routine quantification, monitoring, and evaluation of methane emissions from source regions distributed globally.

RESULTS

Satellite observations of the Permian methane anomaly

Figure 1A shows a map of column-averaged dry-air methane mixing ratio over the conterminous United States, retrieved from TROPOMI measurements, with correction for the topography effect (denoted

as XCH_4^t; see Materials and Methods). The data are averaged from May 2018 to March 2019. Substantial enhancements of XCH_4^t relative to the surrounding background, up to ~30 ppbv, are found over the Permian Basin, indicating strong methane emissions. Other notable enhancements are observed in California's central valley, coastal Southeast, and the Mississippi River Valley, likely associated with anthropogenic (agriculture, dairy) and natural (wetland) sources. The elevated methane levels in central California were also seen earlier in the SCIAMACHY analysis (10).
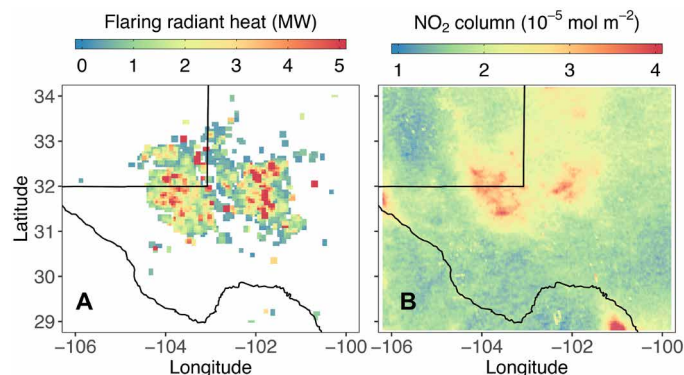
The methane enhancements over the Permian Basin show a characteristic two-branch pattern, which aligns with the two major O/G production sub-basins, the Delaware basin to the west and the Midland basin to the east (Fig. 1B). The enhancement over the Delaware basin, where extensive new exploitation has taken place during the last 5 years (18) (fig. S1), is larger than that over the Midland basin (Fig. 1B). Intensive O/G production activity in these two sub-basins is also captured by satellite observations of radiant heat from gas flaring [Fig. 3A; nighttime observations by the Visible Infrared Imaging Radiometer Suite (VIIRS)] a nd NO_2 tropospheric column densities (Fig. 3B; daytime observations by TROPOMI). Flaring is a common practice in O/G operations to burn off unwanted or excess gas, and NO_2 is a gaseous pollutant released during gas flaring and other combustion activities in O/G fields (19, 20). On the basis of measurements by the VIIRS instrument onboard the Suomi National Polar-orbiting Partnership satellite, we estimate an average flaring rate of 5.9 ± 1.2 billion $m^3 a^{-1}$ during the period of this study, about 4.6% of the gross gas production (see text S1). A fourfold increase in flaring intensity since 2012, observed by the VIIRS instrument, is indicative of the rapid growth in O/G production across the Permian Basin (fig. S1).
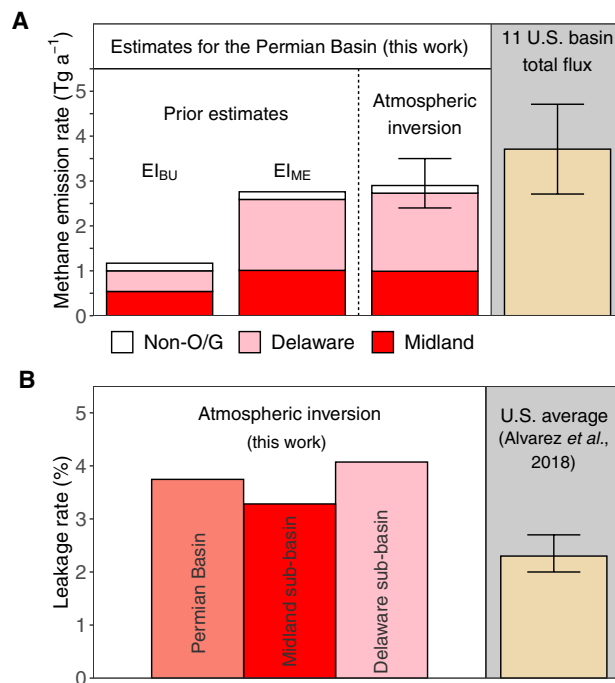
Methane emission quantification

We quantify the methane emission rate from the Permian Basin and its spatial distribution with atmospheric inverse modeling, which optimizes spatially resolved methane emission rates by drawing information from TROPOMI observations and the prior emission estimate following the Bayesian rule. The inversion seeks to optimize monthly methane emission rates resolved at $0.25° \times 0.3125°$ horizontal resolution in a study domain containing the Permian Basin and the surrounding region ($29°–34°N$, $100°–106°W$). The solution to the

optimization is found analytically with closed-form characterization of the error statistics (3). An atmospheric transport model (a nested version of GEOS-Chem over North America with a $0.25° \times 0.3125°$ horizontal resolution) (21) is used as the forward model to relate atmospheric methane columns with ground-level emissions in the study domain and the contributions from outside the domain. The optimization by the inversion significantly reduces the observation-model mismatch with decreased root mean square error (prior, 23 ppbv; posterior, 14 ppbv) and increased correlation (R; prior, 0.30; posterior, 0.62) (fig. S2). See Materials and Methods for more details about the configurations of the inverse modeling including error accounting and prior information.

When aggregating monthly spatially resolved posterior emissions to the basin-level annual average, we find a methane emission flux of 2.9 ± 0.5 Tg a^{-1} from the Permian Basin ($30°–34°N$, $101°–105°W$) (Fig. 4A; see Materials and Methods for the uncertainty analysis). This estimate is more than a factor of 2 larger than the bottom-up estimate based on an extrapolation of EPA greenhouse gas inventory data (EI_{BU}, 1.2 Tg a^{-1}; see Materials and Methods) (Fig. 4A), suggesting that current methane emissions in the Permian are under-represented in national bottom-up emission inventories (22). Our inversion result is in close agreement with a basin-level estimate based on extrapolation of limited ground-based site-level measurements in the Permian (EI_{ME}, 2.8 Tg a^{-1}) (Fig. 4A). It should be noted that these site-level measurements were primarily conducted in the New Mexico portion of the Permian Basin and covered only a

Fig. 4. Methane emission quantification for the Permian Basin. (**A**) Annual methane emissions from the Permian Basin from two prior emission inventories (EI_{BU} and EI_{ME}), and TROPOMI satellite data–based atmospheric inversion and a mass balance method. The breakdown for Delaware, Midland, and non-O/G sources is shown in pink, red, and white for EI_{BU}, EI_{ME}, and atmospheric inversion, respectively. The estimate for the Permian Basin is compared with total emissions from 11 U.S. basins reported in literature (7, 24, 25) (table S1). (**B**) Leakage rates for the Permian Basin and two sub-basins, in comparison with the average leakage reported for the entire United States (7).

Fig. 3. Satellite observations of gas flaring radiant heat and NO_2 tropospheric column density over the Permian Basin. (**A**) Gas flaring radiant heat is the annual average of 2018 measured by the VIIRS satellite instrument, and (**B**) NO_2 tropospheric column density is the 3-month average (June, July, and August of 2018) measured by the TROPOMI instrument, indicating colocated hot spots over the Delaware and Midland sub-basins.

small fraction of production sites (see Materials and Methods and text S2). As a comparison, we also apply a fast mass balance method following Buchwitz *et al.* (*23*) to estimate basin-level emissions, which yields an annual mean emission rate of 3.2 ± 2.0 Tg a^{-1} for the Permian Basin. This result is consistent with that derived from a full atmospheric inversion. Despite the large uncertainty of the mass balance method, this data-driven approach provides an independent estimate of emissions derived primarily using TROPOMI data (see text S3 for more discussion).

Removing the non-O/G sources (0.2 Tg a^{-1}) from the total flux obtained via the inversion (2.9 Tg a^{-1}), we estimate the methane emissions related to O/G activity to be 2.7 Tg a^{-1} in the Permian Basin. Put in the context of national emissions, this value is approximately one quarter of total emissions from all U.S. oil and gas production areas in 2015 (10.9 Tg a^{-1}, including emissions from production, gathering, and processing, which largely occur in the production areas) (*7*). Our estimated emission rate for the Permian is significantly higher than those reported in the literature for other major U.S. O/G-producing basins. Table S1 summarizes methane emission estimates for 11 U.S. basins (*7*, *24*, *25*) from previous aircraft-based studies [i.e., Haynesville (*24*, *26*), Barnett (*24*, *27*), Northeast Pennsylvania (*26*, *28*), Southwest Pennsylvania (*25*), San Juan (*12*), Fayetteville (*26*, *29*), Bakken (*24*, *30*), Uinta (*31*), Weld (*32*), West Arkoma (*26*), Eagle Ford (*24*), and the Denver Basin (*24*)]. Our estimate for the Permian (2.7 Tg a^{-1}) is about a factor of 4 higher than the largest methane emissions from these previously reported O/G basins [i.e., Eagle Ford, 0.73 Tg a^{-1} (*24*)] and is even comparable to the 11-basin sum (3.7 Tg a^{-1}) (Fig. 4A and table S1). This comparison with recent literature indicates that the Permian Basin is likely the largest observed methane-emitting O/G basin in the United States and a substantial contributor to national O/G-related emissions.

Distribution of methane emissions

High-resolution observations from TROPOMI enable us to resolve methane emissions at an unprecedented spatial and temporal resolution, relative to the previous generation of satellite instruments such as the Greenhouse gases Observing SATellite (GOSAT) and SCIAMACHY (*9*). Figure 5 presents the spatial distribution of methane emissions in the Permian Basin at about a quarter-degree resolution derived from our atmospheric inversion. Compared to the prior inventory EI$_{BU}$, our inversion finds larger methane emissions near the center of the Delaware and Midland sub-basins. Sensitivity inversions further show that this spatial pattern is robust against prior emissions of varied magnitudes and distributions (fig. S3), demonstrating that it is primarily informed by satellite observations.

The spatial distribution of methane emissions derived from inversion is closely correlated with that of gross gas production ($R = 0.78$), but to a lesser degree with that of oil production ($R = 0.53$) and that of the well number density ($R = 0.31$) (fig. S4). Similarly, when we sum up the O/G-related emissions for two sub-basins, the ratio of methane emissions between Delaware and Midland (1.7/1.0 Tg a^{-1} = 1.7) is closest to the ratio of gas production (1.4), compared to that of oil production (1.0) and well number density (0.7). Because unconventional wells tend to have much higher production per well than conventional wells (*33*), the dependence of methane emissions on gross gas production rather than the well number density suggests that unconventional wells and infrastructure associated with these wells (e.g., gathering stations), which have been developed recently, are likely the major methane emitters in the Permian Basin.
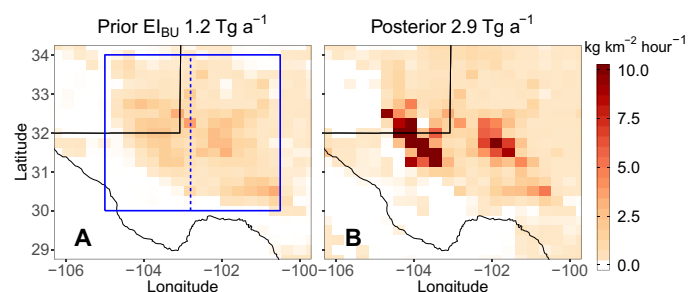
Fig. 5. Spatial distribution of methane emission rates in the Permian Basin. (**A**) Bottom-up emission inventory EI$_{BU}$ extrapolated from EPA greenhouse gas inventory data (prior). (**B**) TROPOMI observation–derived emissions using Bayesian atmospheric inverse modeling (posterior). The prior and posterior basin-total emissions, indicated on top of the figure, are computed over the area enclosed by the solid blue boundary, with contributions from two sub-basins, the Delaware (left of the dashed line) and Midland (right of the dashed line).

In addition to the spatial distribution, our monthly inversion also provides information about the temporal variation of methane emissions during the 11 months of observation (fig. S5). Although the inversion's ability to resolve the spatial distribution of emissions varies from month to month because of uneven monthly sampling of TROPOMI (fig. S5), our inversion ensemble (table S2 and fig. S5) generally results in consistent monthly basin-level emission estimates (see also uncertainty analysis in Materials and Methods). We speculate that high emissions in December 2018 may be related to a very low in-basin gas price toward the end of 2018, resulting from insufficient gas gathering and transmission capacity in the Permian Basin (*33*, *34*). That said, we do not find an apparent increasing trend in methane emissions, although natural gas production from the Permian Basin increased steadily by ~20% during the overlapping 11-month period (fig. S6). Further investigation is required to delineate factors controlling the temporal variations of O/G-related methane emissions.

DISCUSSION
Using an inverse analysis of TROPOMI satellite observations, we estimate a total methane flux of 2.9 ± 0.5 Tg a^{-1} in the Permian Basin, with 2.7 Tg a^{-1} coming from O/G-related activity. Methane losses of this magnitude represent a waste of an important resource; for instance, this is enough natural gas to supply 7 million households in the state of Texas (*35*). Moreover, the 2.7 Tg a^{-1} methane emitted in Permian results in the same radiative forcing as ~260 Tg a^{-1} CO$_2$ over a 20-year time horizon (86 Tg CO$_2$ a^{-1} over a 100-year time horizon) (global warming potential of 96 for 20 years and 32 for 100 years) (*7*, *36*), about the same as annual CO$_2$ emissions from the entire U.S. residential sector (290 Tg CO$_2$ a^{-1} in 2017) (*22*).

Our estimate (2.7 Tg a^{-1}) equates to a production-normalized (73 Tg CH$_4$ a^{-1}, derived from 127 m^3 a^{-1} natural gas production during the study period using 80% methane content by volume) emission rate (or methane leakage rate) of 3.7 ± 0.7%, which is ~60% higher than the national average of 2.3 ± 0.3% (*7*) (Fig. 4B). The leakage rate is even higher for the rapidly developing Delaware sub-basin (4.1%). Comparable high leakage rates have also been reported in other oil production–focused basins such as the Bakken (*24*) (table S1), but these basins produce much lower natural gas than the Permian Basin does. Previous studies summarized in table

S1 show an inverse relationship between the basin-level leakage rate and gas production (*24*); however, the Permian Basin is an outlier with high oil production, high gas production, and a high leakage rate.

Overall, the high leakage rate in the Permian Basin appears to be associated with insufficient infrastructure for natural gas gathering, processing, and transportation (*34*, *37*), leading to extensive venting and flaring (Fig. 3), which contributes to high methane emissions. The greater profitability of oil production contributes to a lack of investment in natural gas takeaway capacity, which, in turn, has resulted in excessive supply of associated gas and a very low in-basin gas price in the Permian (*34*). In addition, with the rescinding of U.S. federal requirements on gas capture and fugitive emissions in 2018, current regulations on O/G methane emissions in the Permian Basin are less stringent at both federal and state levels (see text S4). All these factors may increase the incentive for operators to vent and flare their product. On the other hand, the higher-than-average leakage rate in the Permian Basin implies an opportunity to reduce methane emissions in this rapidly growing oil and gas–producing region, through better design, effective management, regulation, and infrastructure development.

MATERIALS AND METHODS
TROPOMI methane observations
We use daily column-averaged dry air column methane mixing ratio (XCH_4) data retrieved from TROPOMI measurements (*38*) between May 2018 and March 2019. TROPOMI, onboard the polar-orbiting Sentinel-5 Precursor satellite, is a push-broom imaging spectrometer that provides near-daily global coverage with a swath width of 2600 km and a nadir ground pixel size of 7 km × 7 km at approximately 13:30 local overpass time (*17*). The retrieval algorithm accounts for the "full physics" of the light path by simultaneously inferring methane concentrations and physical scattering properties, using the oxygen A-band in the near infrared (NIR) and the methane absorption band in the short-wave infrared (SWIR) (*39*). Only high-quality XCH_4 measurements retrieved under cloud-free conditions are used in this study (as indicated by the retrieval quality assurance flags in TROPOMI data product). These measurements are filtered for solar zenith angle (<70°), low viewing zenith angle (<60°), smooth topography (1 SD of surface elevation <80 m within 5-km radius), and low aerosol load (aerosol optical thickness <0.3 in NIR) (*40*).

The TROPOMI XCH_4 product is further corrected for any known retrieval biases (*40*). The errors in the TROPOMI XCH_4 measurements have been assessed against GOSAT XCH_4 data (*38*) and were found to correlate with surface albedo. A global bias correction linearly dependent on surface albedo was then derived and applied to the TROPOMI data (*40*). This bias-corrected TROPOMI XCH_4 product is used in this study. Negligible correlation of errors with other retrieved parameters (e.g., aerosol optical thickness) was found in the assessment. Validation with independent ground-based measurements from the Total Column Carbon Observing Network shows that the bias-corrected TROPOMI XCH_4 has a bias of −4.3 ± 7.4 ppbv, improved upon the uncorrected XCH_4 product (−12 ± 11.5 ppbv) (*40*). In addition, we also examine the correlation between bias-corrected XCH_4 and other retrieved parameters for the subset of TROPOMI data over the domain of this study. We find no correlation with albedo ($R^2 = 0.00$) and a negligible correlation with aerosol optical thickness ($R^2 = 0.07$), supporting the idea that the XCH_4 enhancement over the Permian Basin (Fig. 1B) is robust.

Figure S7A shows the average XCH_4 over the conterminous United States and the Permian Basin between May 2018 and March 2019 before the topographical correction. We derive the elevation-corrected methane column (XCH_4^t) shown in Fig. 1 by applying a third-order polynomial correction fitted over the U.S. domain following Kort *et al.* (*10*). The mass balance method uses the elevation-corrected data (XCH_4^t) for emission quantification, while the inversion method uses XCH_4 (bias-corrected) directly obtained from the data product, because the topography effect is taken care of by the atmospheric transport model.

Atmospheric inverse modeling
We perform an inverse analysis of TROPOMI observations to derive optimized estimation of monthly methane emissions at 0.25° × 0.3125° horizontal resolution in the Permian Basin. Quantification of emissions at this combination of relatively high spatial and temporal resolution, not achievable with previous generations of satellite observations such as from GOSAT or SCIAMACHY, is enabled by higher-resolution TROPOMI satellite observations (*41*). Figure S7B shows that the Permian Basin is well sampled by TROPOMI during the study period, likely because of frequent cloud-free conditions in the region. A total of ~200,000 TROPOMI XCH_4 retrievals within the study domain (29°–34°N, 100°–106°W) between May 2018 and March 2019 are used for the inversion.

Let $\boldsymbol{x}$ be the state vector that we seek to optimize through inversion, including a gridded ensemble of methane emissions and an additional element representing the regional model bias in XCH_4. The regional model bias term (a monthly scalar uniform over the inversion domain) is necessary to account for spatially uniform biases caused by imperfect lateral boundary condition and emission errors outside the study domain. The inversion solves for an optimal estimate of $\boldsymbol{x}$ by minimizing the following cost function

$$J(\boldsymbol{x}) = (\boldsymbol{x} - \boldsymbol{x}_A)^T \mathbf{S}_A^{-1}(\boldsymbol{x} - \boldsymbol{x}_A) + (\boldsymbol{y} - \mathbf{K}\boldsymbol{x})^T \mathbf{S}_O^{-1}(\boldsymbol{y} - \mathbf{K}\boldsymbol{x}) \quad (1)$$

where TROPOMI XCH_4 observations are assembled in $\boldsymbol{y}$, $\boldsymbol{x}_A$ is the prior estimate of $\boldsymbol{x}$, $\mathbf{S}_A$ is the prior error covariance matrix, $\mathbf{S}_O$ is the observational error covariance matrix, and $\mathbf{K}$ is the Jacobian matrix describing the sensitivity of XCH_4 to emissions and the regional model bias ($\partial \boldsymbol{y}/\partial \boldsymbol{x}$).

Minimization of Eq. 1 at $\nabla_x J(\boldsymbol{x}) = 0$ yields the posterior estimation ($\hat{\boldsymbol{x}}$), the posterior error covariance matrix ($\hat{\mathbf{S}}$), and the averaging kernel matrix ($\mathbf{A}$) (*42*)

$$\hat{\boldsymbol{x}} = \boldsymbol{x}_A + \mathbf{S}_A \mathbf{K}^T (\mathbf{K}\mathbf{S}_A \mathbf{K}^T + \mathbf{S}_O)^{-1}(\boldsymbol{y} - \mathbf{K}\boldsymbol{x}_A) \quad (2)$$

$$\hat{\mathbf{S}} = (\mathbf{K}^T \mathbf{S}_O^{-1} \mathbf{K} + \mathbf{S}_A^{-1})^{-1} \quad (3)$$

$$\mathbf{A} = \mathbf{I}_n - \hat{\mathbf{S}} \mathbf{S}_A^{-1} \quad (4)$$

Here, $\mathbf{I}_n$ is an identity matrix where n is the dimension of the state vector $\boldsymbol{x}$. The trace of $\mathbf{A}$, often called as the degrees of freedom for signal (DOFS), quantifies the number of pieces of information constraining the n-dimensional state vector.

To solve for Eqs. 2 to 4, the prior estimate ($\boldsymbol{x}_A$) for gridded methane emissions is required. Using different sources of information, we create two gridded emission inventories for the study region: one based on bottom-up information (EI_{BU}) and the other based on extrapolation

of ground-based site-level measurements (EI_{ME}) (see below for descriptions of the inventories). Both emission inventories are time invariant. We use EI_{BU} as the prior estimate in the base inversion, while we use EI_{ME} in a sensitivity inversion to evaluate the impact of the prior estimate (PI_EI$_{ME}$; see table S2). We perform further evaluations using prior emissions constructed by disaggregating the total O/G-related emission flux from EI_{BU} with varied spatial proxies (i.e., well count, PI_EI$_{well}$, natural gas production, PI_EI$_{gas}$, and oil production, PI_EI$_{oil}$) (table S2 and fig. S3).

The difference between the EI_{BU} and EI_{ME} (Fig. 5A and fig. S3A) measures the uncertainty of our prior knowledge, and we thus specify prior errors (S_A) for emissions as the absolute difference between EI_{BU} and EI_{ME}. We also specify the prior error for the regional model XCH_4 bias as 10 ppbv. To test the sensitivity to prior errors, we perturb S_A in two sensitivity inversions by doubling (PE × 2) or halving (PE × 0.5) prior errors (table S2). S_O is constructed with the residual error method (43), which results in an error averaged at ~11 ppbv. Both S_O and S_A are taken to be diagonal matrices. We also perform a sensitivity inversion to test the impact of error correlations with off-diagonal terms specified following Cusworth et al. (44) (OE_Cor; see table S2).

A nested version of the GEOS-Chem chemical transport model (12.1.0) is used as the forward model in the inversion to link XCH_4 to surface emissions. To account for the vertical sensitivity of the satellite instrument, we compute simulated XCH_4 by applying TROPOMI averaging kernels to simulated methane vertical profiles. We construct the Jacobian matrix K, column by column, with simulations perturbing each state vector element independently. The simulations are performed over North America and adjacent oceans driven by GEOS-FP–assimilated meteorological data from the NASA Global Modeling and Assimilation Office on a 0.25° × 0.3125° horizontal grid and 47 vertical layers (~30 layers in the troposphere) (21). The boundary conditions for the nested-grid simulation are from a 4° × 5° global simulation from May 2018 to March 2019 driven by GEOS-FP meteorological fields. Note that methane emissions and sinks used in this simulation are optimized with previous-year (2010–2017) GOSAT satellite data following Maasakkers et al. (3). Such generated boundary conditions may be biased (i.e., unable to capture the growth of global methane concentrations; see fig. S9), and we account for it by introducing a monthly regional model bias term in the inversion. The retrieved regional model biases may vary with the extent of the inversion domain. To test this sensitivity, we also perform an inversion with a larger spatial domain (27°–36°N, 98°–108°W) (Bg_Large; see table S2).

Inversion uncertainty

The posterior error covariance matrix ($\hat{S}$, Eq. 2) and averaging kernel matrix (A, Eq. 3) evaluate the uncertainty of an inversion solution given inversion parameters (e.g., S_A, S_O, forward model). Figure S5 shows monthly posterior errors for basin-level emissions (derived from $\hat{S}$) and corresponding DOFS (trace of A) from our base inversion. Overall, the posterior errors for basin-level emissions are <5% of the estimated emission flux, and the DOFS are between 5 and 30 for the monthly inversion, indicating that the TROPOMI data are able to constrain basin-level methane emissions and partially resolve the spatial distribution on a monthly basis. The monthly variations in the posterior error and DOFS are mainly driven by uneven data coverage from TROPOMI sampling. For example, poor data coverage

in November 2018 results in a large posterior error and a small DOFS (fig. S5).

We also perform an ensemble of sensitivity inversions by perturbing the configurations and parameters in the base inversion (table S2), aiming to characterize the uncertainties resulting from assumptions made in the inversion not captured by the analytical posterior error. Our results show that all these sensitivity inversions lead to consistent basin-level emission estimates. Annual mean fluxes from sensitivity inversions are within 0.5 Tg a^{-1} of that from our base inversion (table S2), with general agreement in monthly variations as well (fig. S5). Because the uncertainty resulting from sensitivity inversions are significantly larger than that deduced from posterior error covariance matrix (fig. S5), we report the uncertainty of our basin-level emission estimate (0.5 Tg a^{-1}) as half of the range from the inversion ensemble (2.4 to 3.4 Tg a^{-1}).

Furthermore, to assess the uncertainty due to model transport, we compare hourly GEOS-FP 10-m wind speed against measurements at the Midland Airport (MAF) in the Permian Basin during the period of May 2018 and March 2019. Airport wind measurements are not assimilated in the GEOS-FP reanalysis (45), so these observations are independent. We find that the GEOS-FP 10-m wind speed compares well with the airport measurements in both daytime and nighttime (fig. S8), with mean biases of less than 6% in the mean wind speed. We conclude that errors in the model wind fields are unlikely to be a major source of error in the inversion.

We introduced a regional model bias term in monthly inversions to correct for regional background biases in simulated methane concentrations, which result mainly from imperfect boundary conditions. To check our estimate for this regional bias term, we sample the model simulation to compare with independent observations, i.e., surface measurements at the Mauna Loa Observatory (MLO; a Pacific free tropospheric site upwind of the North American continent) (46), tower measurements at Moody, Texas (WKT) (47), and aircraft measurements offshore Corpus Christi, Texas (TGC) (48). The latter two sites are geographically much closer to the Permian Basin (~400 km from WKT and ~700 km from TGC) than MLO, but can be affected by local emissions that are not optimized in our inversion. Our results show that the model simulation, when corrected with monthly regional model biases (derived from monthly inversions over the Permian Basin), is able to capture the observed monthly variation in methane concentrations, notably the sharp increase from August to October 2018 in MLO and WKT observations (fig. S9), supporting that it is necessary to optimize the regional model bias in the inversion. Better agreement is observed at MLO and TGC compared to WKT (fig. S9), likely because WKT is located closer to local sources that are not fully optimized in the inversion. Overall, most of the differences between the prior simulation and TROPOMI observations can be explained by the regional model biases, except for the mismatch in the vicinity of the Permian Basin (fig. S2). We further perform a sensitivity inversion with a varied spatial domain (Bg_Large). Compared to the base inversion, Bg_Large results in a lower regional methane background (by 3 ppbv on average) and a higher methane emission flux (3.4 Tg a^{-1}) (table S2 and fig. S5), reflecting the error correlation between regional methane biases and methane emissions.

In addition, we note that the inversion cannot fully explain the methane enhancement extending outside the Delaware Basin in the northwest direction (near 33°N, 105°W), although the inversion overall substantially improves the agreement between observations

and model simulations (fig. S2). While our investigations do not attribute an obvious source of emissions causing the northwestern enhancement (whether oil/gas or other sources), the basin-level O/G emission estimates presented here are robust if this enhancement is caused by non-O/G sources, but are conservative if it is caused by O/G sources.

Emission inventory based on bottom-up information

We create a bottom-up methane emission estimate (EI_{BU}) for the study domain starting from the gridded version of the EPA anthropogenic greenhouse gas emission inventory for 2012 (49). Maasakkers et al. (49) developed a procedure to spatially and temporally allocate the national sectorial methane emissions reported in the U.S. Inventory of Greenhouse Gas Emissions and Sinks (GHGI) by U.S. EPA on a $0.1° \times 0.1°$ grid, using various databases at the state, county, local, and point-source level. The emission inventory includes methane emissions from agriculture, coal mining, natural gas systems, petroleum (oil) systems, waste, and other minor anthropogenic sources.

To reflect the intensifying exploitation activity in recent years in the Permian Basin, we then make an extrapolation of the methane emissions from the oil and gas production sector, using 2018 Enverus Drillinginfo data on well count, well completion, and production (50). To account for the changes in the national average emission factors, we further scale the subsectorial production emissions using the ratio between the latest GHGI (22) and a previous GHGI that Maasakkers et al. (49) was based on (51) for 2013 emissions. The updates result in total methane emissions of 1.2 Tg a^{-1} in the Permian Basin (blue box in Fig. 5A), with 1.0 Tg a^{-1} coming from O/G-related emissions and the remainder mainly from agriculture. We use this updated gridded emission inventory (EI_{BU}) as the prior emission estimate for the inversion. The resulting emissions inventory dataset (EI_{BU} inventory) is publicly available for our study region encompassing the entire Permian Basin (https://doi.org/10.7910/DVN/NWQGHU).

Emission inventory based on site-level emission measurements

An alternative prior estimation of methane emissions is obtained by extrapolating ground-based methane emission measurements from a limited sample of oil and gas production sites in the Permian Basin (primarily in the New Mexico portion of the basin) during July and August 2018 (52). The measurements found a wide range of site-level emission rates, which appear to be associated with the complexity of infrastructure, and were classified into emission rates for simple (with only wellheads and/or pump jacks) versus complex sites (also with storage tanks and/or compressors). Extrapolating these site-level emission rates to the entire Permian gave a basin-level methane emission rate of 2.3 Tg a^{-1} from O/G production. Additional emissions from compressor stations and processing plants are estimated to be 0.22 and 0.14 Tg a^{-1}, respectively, using activity data from Enverus Drillinginfo's midstream infrastructure dataset, facility-level emission factors from literature (53, 54), and blowdown event emission factors from GHGI (22). We then disaggregate the basin-level O/G-related emissions to a $0.1° \times 0.1°$ grid by the spatial distribution of gas production (Fig. 2D). To complete the inventory, non-O/G anthropogenic methane emissions (0.2 Tg a^{-1}) are taken from EI_{BU}. This emission inventory (EI_{ME}), based primarily on extrapolation of limited site-level measurements, provides an alternative prior estimate for the inversion and is used to test the sensitivity of the results to the choice of prior information (fig. S3). See text S2 for detailed infor-

mation regarding the site-level measurements and the extrapolation procedure. The resulting emissions inventory dataset (EI_{ME} inventory) is publicly available for our study region encompassing the entire Permian Basin (https://doi.org/10.7910/DVN/NWQGHU).

SUPPLEMENTARY MATERIALS

Supplementary material for this article is available at http://advances.sciencemag.org/cgi/content/full/6/17/eaaz5120/DC1

REFERENCES AND NOTES

1. D. Shindell, J. C. I. Kuylenstierna, E. Vignati, R. van Dingenen, M. Amann, Z. Klimont, S. C. Anenberg, N. Muller, G. Janssens-Maenhout, F. Raes, J. Schwartz, G. Faluvegi, L. Pozzoli, K. Kupiainen, L. Höglund-Isaksson, L. Emberson, D. Streets, V. Ramanathan, K. Hicks, N. T. K. Oanh, G. Milly, M. Williams, V. Demkine, D. Fowler, Simultaneously mitigating near-term climate change and improving human health and food security. *Science* **335**, 183–189 (2012).

2. G. Myhre, D. Shindell, F.-M. Bréon, W. Collins, J. Fuglestvedt, J. Huang, D. Koch, J.-F. Lamarque, D. Lee, B. Mendoza, T. Nakajima, A. Robock, G. Stephens, T. Takemura, H. Zhang, Anthropogenic and natural radiative forcing, in *Climate Change 2013: The Physical Science Basis. Contribution of Working Group I to the Fifth Assessment Report of the Intergovernmental Panel on Climate Change,* T. F. Stocker, D. Qin, G.-K. Plattner, M. Tignor, S. K. Allen, J. Boschung, A. Nuales, Y. Xia, V. Bex, P. M. Midgley, Eds. (Cambridge Univ. Press, 2013), pp. 659–740.

3. J. D. Maasakkers, D. J. Jacob, M. P. Sulprizio, T. R. Scarpelli, H. Nesser, J.-X. Sheng, Y. Zhang, M. Hersher, A. A. Bloom, K. W. Bowman, J. R. Worden, G. Janssens-Maenhout, R. J. Parker, Global distribution of methane emissions, emission trends, and OH concentrations and trends inferred from an inversion of GOSAT satellite data for 2010–2015. *Atmos. Chem. Phys.* **19**, 7859–7881 (2019).

4. S. Schwietzke, O. A. Sherwood, L. M. P. Bruhwiler, J. B. Miller, G. Etiope, E. J. Dlugokencky, S. E. Michel, V. A. Arling, B. H. Vaughn, J. W. C. White, P. P. Tans, Upward revision of global fossil fuel methane emissions based on isotope database. *Nature* **538**, 88–91 (2016).

5. B. Hmiel, V. V. Petrenko, M. N. Dyonisius, C. Buizert, A. M. Smith, P. F. Place, C. Harth, R. Beaudette, Q. Hua, B. Yang, I. Vimont, S. E. Michel, J. P. Severinghaus, D. Etheridge, T. Bromley, J. Schmitt, X. Faïn, R. F. Weiss, E. Dlugokencky, Preindustrial $^{14}CH_4$ indicates greater anthropogenic fossil CH_4 emissions. *Nature* **578**, 409–412 (2020).

6. R. A. Alvarez, S. W. Pacala, J. J. Winebrake, W. L. Chameides, S. P. Hamburg, Greater focus needed on methane leakage from natural gas infrastructure. *Proc. Natl. Acad. Sci. U.S.A.* **109**, 6435–6440 (2012).

7. R. A. Alvarez, D. Zavala-Araiza, D. R. Lyon, D. T. Allen, Z. R. Barkley, A. R. Brandt, K. J. Davis, S. C. Herndon, D. J. Jacob, A. Karion, E. A. Kort, B. K. Lamb, T. Lauvaux, J. D. Maasakkers, A. J. Marchese, M. Omara, S. W. Pacala, J. Peischl, A. L. Robinson, P. B. Shepson, C. Sweeney, A. Townsend-Small, S. C. Wofsy, S. P. Hamburg, Assessment of methane emissions from the U.S. oil and gas supply chain. *Science* **361**, 186–188 (2018).

8. EPA, Inventory of US greenhouse gas emissions and sinks: 1990–2015 (2017); https://www.epa.gov/ghgemissions/inventory-us-greenhouse-gas-emissions-and-sinks-1990-2015.

9. D. J. Jacob, A. J. Turner, J. D. Maasakkers, J. Sheng, K. Sun, X. Liu, K. Chance, I. Aben, J. McKeever, C. Frankenberg, Satellite observations of atmospheric methane and their value for quantifying methane emissions. *Atmos. Chem. Phys.* **16**, 14371–14396 (2016).

10. E. A. Kort, C. Frankenberg, K. R. Costigan, R. Lindenmaier, M. K. Dubey, D. Wunch, Four corners: The largest US methane anomaly viewed from space. *Geophys. Res. Lett.* **41**, 6898–6903 (2014).

11. C. Frankenberg, A. K. Thorpe, D. R. Thompson, G. Hulley, E. A. Kort, N. Vance, J. Borchardt, T. Krings, K. Gerilowski, C. Sweeney, S. Conley, B. D. Bue, A. D. Aubrey, S. Hook, R. O. Green, Airborne methane remote measurements reveal heavy-tail flux distribution in Four Corners region. *Proc. Natl. Acad. Sci. U.S.A.* **113**, 9734–9739 (2016).

12. M. L. Smith, A. Gvakharia, E. A. Kort, C. Sweeney, S. A. Conley, I. Faloona, T. Newberger, R. Schnell, S. Schwietzke, S. Wolter, Airborne quantification of methane emissions over the four corners region. *Environ. Sci. Technol.* **51**, 5832–5837 (2017).

13. EIA, Drilling productivity report; https://www.eia.gov/petroleum/drilling/ [accessed 1 May 2019].

14. C. Krauss, "The 'monster' Texas oil field that made the U.S. a star in the world market," *New York Times*, 2019.

15. K. A. Willyard, G. W. Schade, Flaring in two Texas shale areas: Comparison of bottom-up with top-down volume estimates for 2012 to 2015. *Sci. Total Environ.* **691**, 243–251 (2019).

16. SRON, S5P Mission Performance Centre Methane [L2__CH4___] Readme, S5P-MPC-SRON-PRF-CH4, V01.03.02 (2019).

17. J. P. Veefkind, I. Aben, K. McMullan, H. Förster, J. de Vries, G. Otter, J. Claas, H. J. Eskes, J. F. de Haan, Q. Kleipool, M. van Weele, O. Hasekamp, R. Hoogeveen, J. Landgraf, R. Snel, P. Tol, P. Ingmann, R. Voors, B. Kruizinga, R. Vink, H. Visser, P. F. Levelt, TROPOMI on the ESA Sentinel-5 Precursor: A GMES mission for global observations of the atmospheric composition for climate, air quality and ozone layer applications. *Remote Sens. Environ.* **120**, 70–83 (2012).

18. EIA, The Wolfcamp play has been key to Permian Basin oil and natural gas production growth (2018); https://www.eia.gov/todayinenergy/detail.php?id=37532#tab1 [accessed 18 August 2019].

19. Y. Zhang, R. Gautam, D. Zavala-Araiza, D. J. Jacob, R. Zhang, L. Zhu, J.-X. Sheng, T. Scarpelli, Satellite-observed changes in Mexico's offshore gas flaring activity linked to oil/gas regulations. *Geophys. Res. Lett.* **46**, 1879–1888 (2019).

20. B. N. Duncan, L. N. Lamsal, A. M. Thompson, Y. Yoshida, Z. Lu, D. G. Streets, M. M. Hurwitz, K. E. Pickering, A space-based, high-resolution view of notable changes in urban NO$_x$ pollution around the world (2005-2014). *J. Geophys. Res. Atmos.* **121**, 976–996 (2016).

21. J. X. Sheng, D. J. Jacob, A. J. Turner, J. D. Maasakkers, M. P. Sulprizio, A. A. Bloom, A. E. Andrews, D. Wunch, High-resolution inversion of methane emissions in the Southeast US using SEAC^{4}RS aircraft observations of atmospheric methane: Anthropogenic and wetland sources. *Atmos. Chem. Phys.* **18**, 6483–6491 (2018).

22. EPA, Inventory of US greenhouse gas emissions and sinks: 1990–2017 (2019); https://www.epa.gov/ghgemissions/inventory-us-greenhouse-gas-emissions-and-sinks-1990-2017.

23. M. Buchwitz, O. Schneising, M. Reuter, J. Heymann, S. Krautwurst, H. Bovensmann, J. P. Burrows, H. Boesch, R. J. Parker, P. Somkuti, R. G. Detmers, O. P. Hasekamp, I. Aben, A. Butz, C. Frankenberg, A. J. Turner, Satellite-derived methane hotspot emission estimates using a fast data-driven method. *Atmos. Chem. Phys.* **17**, 5751–5774 (2017).

24. J. Peischl, S. J. Eilerman, J. A. Neuman, K. C. Aikin, J. de Gouw, J. B. Gilman, S. C. Herndon, R. Nadkarni, M. Trainer, C. Warneke, T. B. Ryerson, Quantifying methane and ethane emissions to the atmosphere from Central and Western U.S. oil and natural gas production regions. *J. Geophys. Res. Atmos.* **123**, 7725–7740 (2018).

25. X. Ren, D. L. Hall, T. Vinciguerra, S. E. Benish, P. R. Stratton, D. Ahn, J. R. Hansford, M. D. Cohen, S. Sahu, H. He, C. Grimes, J. D. Fuentes, P. B. Shepson, R. J. Salawitch, S. H. Ehrman, R. R. Dickerson, Methane emissions from the Marcellus Shale in Southwestern Pennsylvania and Northern West Virginia based on airborne measurements. *J. Geophys. Res. Atmos.* **124**, 1862–1878 (2019).

26. J. Peischl, T. B. Ryerson, K. C. Aikin, J. A. de Gouw, J. B. Gilman, J. S. Holloway, B. M. Lerner, R. Nadkarni, J. A. Neuman, J. B. Nowak, M. Trainer, C. Warneke, D. D. Parrish, Quantifying atmospheric methane emissions from the Haynesville, Fayetteville, and northeastern Marcellus shale gas production regions. *J. Geophys. Res. Atmos.* **120**, 2119–2139 (2015).

27. A. Karion, C. Sweeney, E. A. Kort, P. B. Shepson, A. Brewer, M. Cambaliza, S. A. Conley, K. Davis, A. Deng, M. Hardesty, S. C. Herndon, T. Lauvaux, T. Lavoie, D. Lyon, T. Newberger, G. Pétron, C. Rella, M. Smith, S. Wolter, T. I. Yacovitch, P. Tans, Aircraft-based estimate of total methane emissions from the Barnett Shale region. *Environ. Sci. Technol.* **49**, 8124–8131 (2015).

28. Z. R. Barkley, T. Lauvaux, K. J. Davis, A. Deng, N. L. Miles, S. J. Richardson, Y. Cao, C. Sweeney, A. Karion, M. K. Smith, E. A. Kort, S. Schwietzke, T. Murphy, G. Cervone, D. Martins, J. D. Maasakkers, Quantifying methane emissions from natural gas production in north-eastern Pennsylvania. *Atmos. Chem. Phys.* **17**, 13941–13966 (2017).

29. S. Schwietzke, G. Pétron, S. Conley, C. Pickering, I. Mielke-Maday, E. J. Dlugokencky, P. P. Tans, T. Vaughn, C. Bell, D. Zimmerle, S. Wolter, C. W. King, A. B. White, T. Coleman, L. Bianco, R. C. Schnell, Improved mechanistic understanding of natural gas methane emissions from spatially resolved aircraft measurements. *Environ. Sci. Technol.* **51**, 7286–7294 (2017).

30. J. Peischl, A. Karion, C. Sweeney, E. A. Kort, M. L. Smith, A. R. Brandt, T. Yeskoo, K. C. Aikin, S. A. Conley, A. Gvakharia, M. Trainer, S. Wolter, T. B. Ryerson, Quantifying atmospheric methane emissions from oil and natural gas production in the Bakken shale region of North Dakota. *J. Geophys. Res. Atmos.* **121**, 6101–6111 (2016).

31. A. Karion, C. Sweeney, G. Pétron, G. Frost, R. Michael Hardesty, J. Kofler, B. R. Miller, T. Newberger, S. Wolter, R. Banta, A. Brewer, E. Dlugokencky, P. Lang, S. A. Montzka, R. Schnell, P. Tans, M. Trainer, R. Zamora, S. Conley, Methane emissions estimate from airborne measurements over a western United States natural gas field. *Geophys. Res. Lett.* **40**, 4393–4397 (2013).

32. G. Pétron, A. Karion, C. Sweeney, B. R. Miller, S. A. Montzka, G. J. Frost, M. Trainer, P. Tans, A. Andrews, J. Kofler, D. Helmig, D. Guenther, E. Dlugokencky, P. Lang, T. Newberger, S. Wolter, B. Hall, P. Novelli, A. Brewer, S. Conley, M. Hardesty, R. Banta, A. White, D. Noone, D. Wolfe, R. Schnell, A new look at methane and nonmethane hydrocarbon emissions from oil and natural gas operations in the Colorado Denver-Julesburg Basin. *J. Geophys. Res. Atmos.* **119**, 6836–6852 (2014).

33. M. Omara, M. R. Sullivan, X. Li, R. Subramanian, A. L. Robinson, A. A. Presto, Methane emissions from conventional and unconventional natural gas production sites in the marcellus shale basin. *Environ. Sci. Technol.* **50**, 2099–2107 (2016).

34. RBN Energy, "Hell In Texas—Permian gas takeaway headed for capacity wall," RBN Energy Drill Down Report (2018).

35. EIA, Natural gas consumption by end use; https://www.eia.gov/dnav/ng/ng_cons_sum_dcu_STX_a.htm. [accessed 20 August 2019].

36. M. Etminan, G. Myhre, E. J. Highwood, K. P. Shine, Radiative forcing of carbon dioxide, methane, and nitrous oxide: A significant revision of the methane radiative forcing. *Geophys. Res. Lett.* **43**, 12,614–12,623 (2016).

37. T. Curtis, B. Montalbano, *The Permian Basin Produces Gas, Too—Permian Basin Oil and Gas Production Growth: A Case Study for Gas Infrastructure Needs in the U.S.* (Energy Policy Research Foundation Inc., 2018).

38. H. Hu, J. Landgraf, R. Detmers, T. Borsdorff, J. aan de Brugh, I. Aben, A. Butz, O. Hasekamp, Toward global mapping of methane with TROPOMI: First results and intersatellite comparison to GOSAT. *Geophys. Res. Lett.* **45**, 3682–3689 (2018).

39. H. Hu, O. Hasekamp, A. Butz, A. Galli, J. Landgraf, J. Aan de Brugh, T. Borsdorff, R. Scheepmaker, I. Aben, The operational methane retrieval algorithm for TROPOMI. *Atmos. Meas. Tech.* **9**, 5423–5440 (2016).

40. O. Hasekamp, A. Lorente, H. Hu, A. Butz, J. aan de Brugh, J. Landgraf, "Algorithm theoretical baseline document for Sentinel-5 Precursor methane retrieval (issue 1.10), SRON-S5P-LEV2-RP-001" (SRON, 2019).

41. J.-X. Sheng, D. J. Jacob, J. D. Maasakkers, Y. Zhang, M. P. Sulprizio, Comparative analysis of low-Earth orbit (TROPOMI) and geostationary (GeoCARB, GEO-CAPE) satellite instruments for constraining methane emissions on fine regional scales: Application to the Southeast US. *Atmos. Meas. Tech.* **11**, 6379–6388 (2018).

42. G. P. Brasseur, D. J. Jacob, *Modeling of Atmospheric Chemistry* (Cambridge Univ. Press, 2017).

43. C. L. Heald, D. J. Jacob, D. B. A. Jones, P. I. Palmer, J. A. Logan, D. G. Streets, G. W. Sachse, J. C. Gille, R. N. Hoffman, T. Nehrkorn, Comparative inverse analysis of satellite (MOPITT) and aircraft (TRACE-P) observations to estimate Asian sources of carbon monoxide. *J. Geophys. Res. Atmos.* **109**, D23306 (2004).

44. D. H. Cusworth, D. J. Jacob, J.-X. Sheng, J. Benmergui, A. J. Turner, J. Brandman, L. White, C. A. Randles, Detecting high-emitting methane sources in oil/gas fields using satellite observations. *Atmos. Chem. Phys.* **18**, 16885–16896 (2018).

45. M. M. Rienecker, M. J. Suarez, R. Todling, J. Bacmeister, L. Takacs, H.-C. Liu, W. Gu, M. Sienkiewicz, R. D. Koster, R. Gelaro, I. Stajner, J. E. Nielsen, "The GEOS-5 data assimilation system—Documentation of versions 5.0.1, 5.1.0, and 5.2.0" (NASA Tech. Rep. NASA/TM-2008-104606, NASA, 2008), vol. 27, 118 pp.; https://gmao.gsfc.nasa.gov/pubs/docs/Rienecker369.pdf.

46. E. J. Dlugokencky, A. M. Crotwell, P. M. Lang, J. W. Mund, M. E. Rhodes, Atmospheric methane dry air mole fractions from quasi-continuous measurements at Barrow, Alaska and Mauna Loa, Hawaii, 1986–2017, version: 2019-06-21; ftp://aftp.cmdl.noaa.gov/data/trace_gases/ch4/in-situ/surface/ (2018).

47. A. E. Andrews, J. D. Kofler, M. E. Trudeau, J. C. Williams, D. H. Neff, K. A. Masarie, D. Y. Chao, D. R. Kitzis, P. C. Novelli, C. L. Zhao, E. J. Dlugokencky, P. M. Lang, M. J. Crotwell, M. L. Fischer, M. J. Parker, J. T. Lee, D. D. Baumann, A. R. Desai, C. O. Stanier, S. F. J. De Wekker, D. E. Wolfe, J. W. Munger, P. P. Tans, CO$_2$, CO, and CH$_4$ measurements from tall towers in the NOAA Earth System Research Laboratory's Global Greenhouse Gas Reference Network: Instrumentation, uncertainty analysis, and recommendations for future high-accuracy greenhouse gas monitoring efforts. *Atmos. Meas. Tech.* **7**, 647–687 (2014).

48. C. Sweeney, A. Karion, S. Wolter, T. Newberger, D. Guenther, J. A. Higgs, A. E. Andrews, P. M. Lang, D. Neff, E. Dlugokencky, J. B. Miller, S. A. Montzka, B. R. Miller, K. A. Masarie, S. C. Biraud, P. C. Novelli, M. Crotwell, A. M. Crotwell, K. Thoning, P. P. Tans, Seasonal climatology of CO$_2$ across North America from aircraft measurements in the NOAA/ESRL Global Greenhouse Gas Reference Network. *J. Geophys. Res. Atmos.* **120**, 5155–5190 (2015).

49. J. D. Maasakkers, D. J. Jacob, M. P. Sulprizio, A. J. Turner, M. Weitz, T. Wirth, C. Hight, M. DeFigueiredo, M. Desai, R. Schmeltz, L. Hockstad, A. A. Bloom, K. W. Bowman, S. Jeong, M. L. Fischer, Gridded national inventory of U.S. methane emissions. *Environ. Sci. Technol.* **50**, 13123–13133 (2016).

50. Enverus DrillingInfo, DI Desktop (2019); didesktop.com.

51. EPA, Inventory of US greenhouse gas emissions and sinks: 1990–2014 (2016); https://www.epa.gov/ghgemissions/inventory-us-greenhouse-gas-emissions-and-sinks-1990-2014.

52. EDF, New Mexico oil & gas data (2019); https://www.edf.org/nm-oil-gas/ [accessed 18 August 2019].

53. A. J. Marchese, T. L. Vaughn, D. J. Zimmerle, D. M. Martinez, L. L. Williams, A. L. Robinson, A. L. Mitchell, R. Subramanian, D. S. Tkacik, J. R. Roscioli, S. C. Herndon, Methane emissions from United States natural gas gathering and processing. *Environ. Sci. Technol.* **49**, 10718–10727 (2015).

54. A. L. Mitchell, D. S. Tkacik, J. R. Roscioli, S. C. Herndon, T. I. Yacovitch, D. M. Martinez, T. L. Vaughn, L. L. Williams, M. R. Sullivan, C. Floerchinger, M. Omara, R. Subramanian, D. Zimmerle, A. J. Marchese, A. L. Robinson, Measurements of methane emissions

from natural gas gathering facilities and processing plants: Measurement results. *Environ. Sci. Technol.* **49**, 3219–3227 (2015).

55. C. Elvidge, M. Zhizhin, K. Baugh, F.-C. Hsu, T. Ghosh, Methods for global survey of natural gas flaring from visible infrared imaging radiometer suite data. *Energies* **9**, 14 (2016).

56. A. M. Robertson, R. Edie, D. Snare, J. Soltis, R. A. Field, M. D. Burkhart, C. S. Bell, D. Zimmerle, S. M. Murphy, Variation in methane emission rates from well pads in four oil and gas basins with contrasting production volumes and compositions. *Environ. Sci. Technol.* **51**, 8832–8840 (2017).

57. D. Zavala-Araiza, D. R. Lyon, R. A. Alvarez, K. J. Davis, R. Harriss, S. C. Herndon, A. Karion, E. A. Kort, B. K. Lamb, X. Lan, A. J. Marchese, S. W. Pacala, A. L. Robinson, P. B. Shepson, C. Sweeney, R. Talbot, A. Townsend-Small, T. I. Yacovitch, D. J. Zimmerle, S. P. Hamburg, Reconciling divergent estimates of oil and gas methane emissions. *Proc. Natl. Acad. Sci. U.S.A.* **112**, 15597–15602 (2015).

Citation: Y. Zhang, R. Gautam, S. Pandey, M. Omara, J. D. Maasakkers, P. Sadavarte, D. Lyon, H. Nesser, M. P. Sulprizio, D. J. Varon, R. Zhang, S. Houweling, D. Zavala-Araiza, R. A. Alvarez, A. Lorente, S. P. Hamburg, I. Aben, D. J. Jacob, Quantifying methane emissions from the largest oil-producing basin in the United States from space. *Sci. Adv.* **6**, eaaz5120 (2020).

Science Advances

Quantifying methane emissions from the largest oil-producing basin in the United States from space

Yuzhong Zhang, Ritesh Gautam, Sudhanshu Pandey, Mark Omara, Joannes D. Maasakkers, Pankaj Sadavarte, David Lyon, Hannah Nesser, Melissa P. Sulprizio, Daniel J. Varon, Ruixiong Zhang, Sander Houweling, Daniel Zavala-Araiza, Ramon A. Alvarez, Alba Lorente, Steven P. Hamburg, Ilse Aben and Daniel J. Jacob

ARTICLE TOOLS	http://advances.sciencemag.org/content/6/17/eaaz5120
SUPPLEMENTARY MATERIALS	http://advances.sciencemag.org/content/suppl/2020/04/20/6.17.eaaz5120.DC1
REFERENCES	This article cites 40 articles, 5 of which you can access for free http://advances.sciencemag.org/content/6/17/eaaz5120#BIBL
PERMISSIONS	http://www.sciencemag.org/help/reprints-and-permissions

Use of this article is subject to the Terms of Service